ACS APPLIED MATERIALS & INTERFACES

Research Article

www.acsami.org

Characteristic Work Function Variations of Graphene Line Defects

Fei Long,[†] Poya Yasaei,[‡] Raj Sanoj,[§] Wentao Yao,[†] Petr Král,[§,∥] Amin Salehi-Khojin,*[,‡] and Reza Shahbazian-Yassar*[,†,‡]

[†]Department of Mechanical Engineering and Engineering Mechanics, Michigan Technological University, Houghton, Michigan 49931, United States

[‡]Department of Mechanical and Industrial Engineering, [§]Department of Chemistry, and [∥]Department of Physics and Biopharmaceutical Science, University of Illinois at Chicago, Chicago, Illinois 60607, United States

Supporting Information

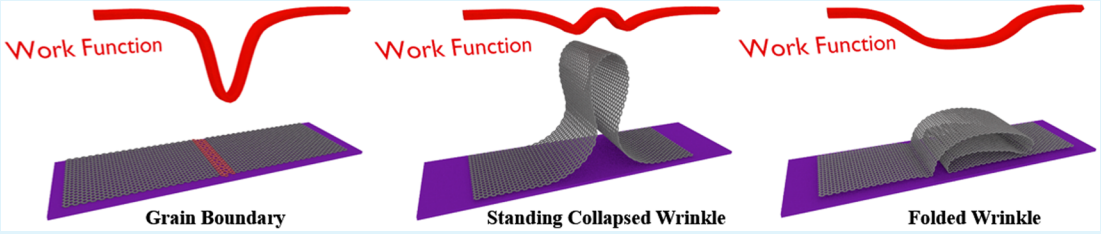

ABSTRACT: Line defects, including grain boundaries and wrinkles, are commonly seen in graphene grown by chemical vapor deposition. These one-dimensional defects are believed to alter the electrical and mechanical properties of graphene. Unfortunately, it is very tedious to directly distinguish grain boundaries from wrinkles due to their similar morphologies. In this report, high-resolution Kelvin potential force microscopy (KPFM) is employed to measure the work function distribution of graphene line defects. The characteristic work function variations of grain boundaries, standing-collapsed wrinkles, and folded wrinkles could be clearly identified. Classical and quantum molecular dynamics simulations reveal that the unique work function distribution of each type of line defects is originated from the doping effect induced by the SiO_2 substrate. Our results suggest that KPFM can be an easy-to-use and accurate method to detect graphene line defects, and also propose the possibility to tune the graphene work function by defect engineering.

KEYWORDS: *graphene, line defects, work function, atomic force microscopy, density functional theory*

1. INTRODUCTION

Growth of large-area graphene by chemical vapor deposition (CVD) is currently the most promising way for practical applications of graphene-based devices.[1] During the growth process, neighboring graphene grains are stitched together through disordered grain boundaries (GBs), resulting in a polycrystalline film. It is widely accepted that GBs alter the electrical and mechanical performance of graphene,[2−4] while demonstrating exciting potential in sensing applications due to a high chemical reactivity.[5] The nonhexagonal carbon rings along GBs usually lead to out-of-plane buckling in order to minimize the strain energy.[6] On the other hand, another type of line defect, "wrinkles", is often observed on CVD-grown graphene films, mainly due to different thermal expansion between graphene and metal substrate.[7−9] Qualitatively speaking, the competition between bending and van der Waals binding energy leads to two types of wrinkles, namely "standing collapsed wrinkles" and "folded wrinkles".[10] The schematic structures of these line defects are illustrated in Figure 1 a−c. Direct visualization of GBs usually requires atomic-resolution scanning tunneling microscopy (STM)[11] and transmission electron microscopy (TEM),[12] but the field of view is limited to tens of nanometers. At micrometer length scale, GBs has been indirectly determined by dark field TEM through mapping of individual grains.[13] However, other types of line defects such as wrinkles cannot be easily captured by this method. Liquid crystal coating[14] and selective oxidation of metallic substrate[15] also can resolve GBs at lager length scale from microns to even millimeters. But these methods requires chemical modifications of either graphene or the substrate. Recently, simultaneous visualization of GBs and wrinkles was achieved by deposition of Au nanoparticles on graphene surface.[16] In this method, the line defects are believed to disrupt the diffusion of nanoparticles, so single-line and double-line patterns could be formed along GBs and wrinkles, respectively. However, the nanoparticle deposition requires carefully selected annealing conditions, and this method also modifies the graphene surface. The destructive nature of the current techniques limits the employment in many applications where direct characterizations of GBs and grains are needed before and after experiments, such as electronic devices and catalyst applications.

Kelvin potential force microscopy (KPFM)[17] can detect the contact potential difference between an AFM probe and the

Received: April 23, 2016
Accepted: June 29, 2016
Published: June 29, 2016

DOI: 10.1021/acsami.6b04853
ACS Appl. Mater. Interfaces 2016, 8, 18360−18366

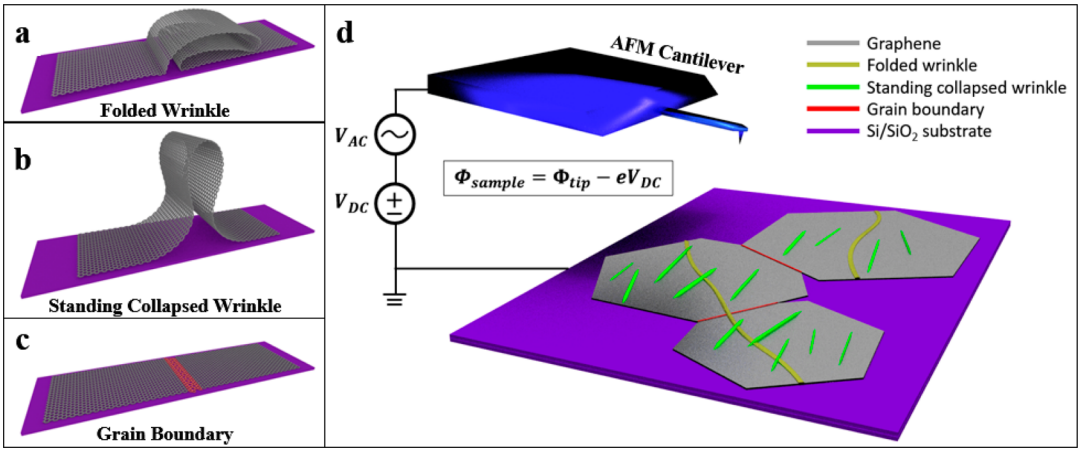

Figure 1. (a–c) Schematic morphology of folded wrinkle, standing collapsed wrinkle, and grain boundary, respectively, on graphene grown by chemical vapor deposition. (d) Experimental setup of KPFM.

sample surface. It has the advantage of contactless electrical mapping down to the nanometer scale.[18] Therefore, it has been widely used to characterize monolayer, bilayer, and multilayer graphene due to substrate-induced work function variations.[19−21] Briefly, during KPFM measurement, the sample is grounded while a bias $\Delta V = V_{DC} + V_{AC}$ is applied to the AFM cantilever, where V_{DC} and V_{AC} are the DC and AC components, respectively, as shown in Figure 1d. The frequency of V_{AC} is chosen at the resonant frequency of the cantilever. The AFM controller nulls the cantilever amplitude due to periodic electrostatic force by adjusting V_{DC}. If the work function of the cantilever tip Φ_{tip} is known, then the sample work function Φ_s can be given as $\Phi_s = \Phi_{tip} - eV_{DC}$. The variables Φ_s and V_{DC} are opposite in sign, so the work function Φ_s has inverse contrast with KPFM mapping.

Although line defects such as GBs and wrinkles are believed to modify the local electrical properties of graphene, to our best knowledge, no KPFM study on CVD graphene defects has been reported. One probable reason could be the low spatial resolution in the work function mapping due to the parasitic electrostatic contribution of the relatively large cantilevers (up to hundreds of microns), which leads to the averaging of signals. To suppress this averaging effect[22] and increase the spatial resolution of KPFM, AFM probes with much smaller cantilever size are selected in our experiments. As a result, we successfully achieved enough resolution for surface potential mapping of graphene line defects (see Methods).

In this study, the graphene samples are synthesized on copper foils by the ambient pressure CVD technique,[4,23] and then transferred on Si/SiO_2 substrate using the poly(methyl methacrylate) (PMMA)-assisted technique as previously described.[5] Scanning electron microscopy (SEM) and Raman spectroscopy are employed to check the sample morphology and defects before KPFM measurements.

2. METHODS

2.1. Synthesis Process. The graphene growth was carried out in an ambient-pressure chemical vapor deposition (AP-CVD) method, similar to our previous reports.[5,24] In this approach, single crystalline graphene flakes with predominant zigzag edges grow discretely and eventually merge together forming grain boundaries. In short, the synthesis process starts with preparation of the copper substrates (Alfa Aesar, product 46365). The foils were initially treated for 10−20 min in 10% hydrochloric acid (in deionized water), rinsed in acetone and isopropanol, dried under N_2 flow, and loaded into the CVD chamber. The chamber was then evacuated (to 1 mTorr) and then purged with forming gas (5% hydrogen diluted in Ar) to the atmospheric pressure. The samples were heated to 1050 °C under the same flow for 60 min. Next, 20 ppm of methane (CH_4) was introduced for 40−90 min (depending on the desired surface coverage). The chamber was then quenched and samples were taken out for characterization. The as-grown graphene films were then coated with PMMA and floated on copper etchant (CE-100). After 24 h, the copper was completely dissolved and the samples were transferred to several other DI water baths to remove the solvent residue. A bath of 5% hydrochloric acid was also used to remove the etchant residue. Finally, the floating samples were scooped out by the target (Si/SiO_2) substrates and annealed in vacuum at 350 °C for 2 h under flow of 5% forming gas to remove the polymer residue and enhance the adhesion to the surface.

2.2. AFM Experiment. All AFM experiments were carried out with Dimension ICON system (Bruker, CA) in ambient conditions. PFQNE-AL cantilevers (Bruker, CA) were selected for the improved spatial resolution in surface potential measurements. The nominal spring constant was 0.8 N/m and resonant frequency was 300 kHz. Two-pass technique (also known as "liftmode") was applied in KPFM experiments. In the first pass, the AFM scanned the surface in tapping mode and the line profile of the topography was recorded; the tapping amplitude was estimated to be 4−6 nm. In the second pass, a bias $\Delta V = V_{DC} + V_{AC}$ was applied to the AFM cantilever, where V_{DC} and V_{AC} are the DC and AC components, respectively. The frequency of V_{AC} was chosen at the resonant frequency of the cantilever. The AFM scanner lifted the tip ∼10 nm away from the surface, and scanned the sample in parallel fashion with respect to the recorded line profile. This two-pass technique can effectively remove the artifacts induced by topography, thereby increasing the resolution and accuracy of the electrical measurement.

2.3. SEM. All SEM images were obtained with an integrated Carl Zeiss microscope in a Raith e-LiNE plus electron beam lithography system. We used the acceleration voltage of 10 kV and working distance of 10 mm for imaging.

2.4. Raman Spectroscopy. The Raman spectra were obtained with a Horiba LabRAM HR Evolution confocal Raman microscope with a 532 nm laser wavelength, 1200 g/mm grating, and a 100× objective lens. The laser power was in the range of 1−4 mW.

2.5. Molecular Dynamics Simulation. The classical molecular dynamics (MD) simulations were performed with NAMD[25,26] and the CHARMM32 force field.[27] The temperature was kept fixed at $T = 300$ K in our simulation by the Langevin dynamics. The switching distance for nonbonded interactions was set to 7 Å, and the cutoff was set to 10 Å. The systems were simulated in an NVT ensemble (the ensemble with constant number of particles, constant volume, and constant temperature), where the particle mesh Ewald summation[28] was used to describe a long-range Columbic coupling. Quantum MD simulations were performed using TeraChem[29−31] with restricted Hartree−Fock

DOI: 10.1021/acsami.6b04853
ACS Appl. Mater. Interfaces 2016, 8, 18360−18366

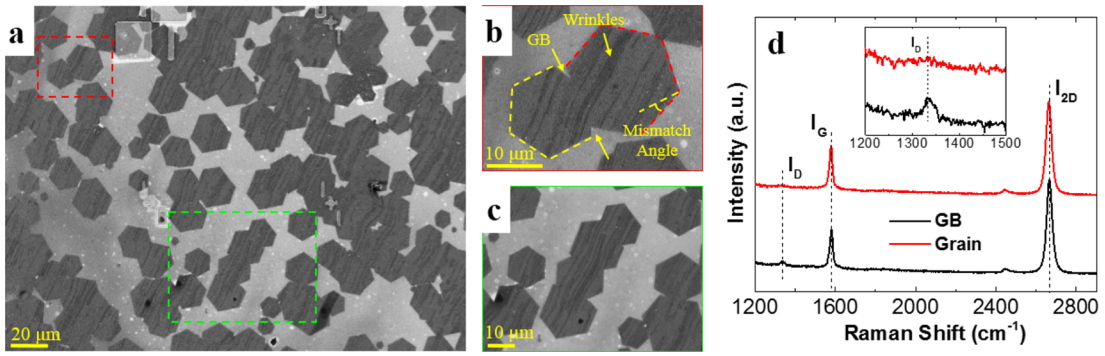

Figure 2. (a) Typical SEM image of CVD-grown graphene after transfer on Si/SiO_2 substrate. The hexagonal morphology indicates the single-crystalline nature of individual graphene flakes. (b) Coalescence of two grains with nonzero mismatch angle. The grain boundary is indicated with arrows. Wrinkles can also be observed as darker contrast strips. (c) Coalescence of four grains. (d) Two Raman spectra obtained from the single crystalline graphene and the GB region. Both of them have I_{2D}/I_G ratios of ~2, which is characteristic for monolayer graphene. The inset magnifies the same spectra at ~1350 cm^{-1}, which shows the dislocation-induced D peak.

(RHF) with a 3-21g basis set. To describe nonbonded interactions, we performed the calculations with dispersion corrections (the revised DFT-D method), as implemented in TeraChem. The atomic charges in these systems were calculated within the Mulliken scheme. The simulation procedures were as follows. First, we deposited all three uncharged systems on amorphous SiO_2 prepared by visual molecular dynamics (VMD) and ran the simulations for ~10 ns. Upon equilibrium, we took the systems and performed density functional theory (DFT) calculation for each system separately. The calculations revealed that different systems are differently doped by SiO_2 due to their atomic structures. The atomic charges were then used to calculate the electrostatic potential. A short Fortran code was written to calculate the potential as a function of position.

3. RESULTS AND DISCUSSION

As shown in Figure 2a, the large-area SEM image shows partially covered individual hexagonal graphene grains. In these samples, the location of the GBs can be estimated from the geometry of the as-grown grains that is in the merging regions of the hexagons. Additionally, it is known that the edges of the hexagonal flakes in this CVD grown samples are mostly aligned with zigzag crystalline orientation of the grains due to their higher chemical stability in the growth process.[4,5] This can be used to estimate the crystalline misorientation of the grains, as also demonstrated in Figure 2b. In SEM images, where the wrinkle-rich area appears as darker strips, the GBs could not be directly resolved. To confirm the existence of GBs in the merging regions of the hexagons, we performed Raman point spectroscopy in the middle of the hexagons and in their merging region (Figure 2d). The inset in Figure 2d shows an enhanced D peak signal at 1350 cm^{-1}, which is due to dislocations within the GB region. It worth noting that the I_{2D}/I_G ratios of both spectra are close to 2, indicating that the graphene sample is monolayer.

Tapping mode topography is shown in Figure 3a, where two grains coalesced with ~43° tilt angle as indicated. The surface morphology displays a high density of wrinkles with three of them highlighted by blue arrows. The heights of these wrinkles vary from 1 to 5 nm, and they almost align along the same direction. These wrinkles are referred to as "standing collapsed wrinkles"[10] in the following context. Meanwhile, another type of line defect is observed as indicated by the yellow arrow. Its direction is no longer parallel with the standing collapsed wrinkles, and the height of this line is approximately 0.5−0.9 nm along its length, which is in good agreement with bilayer graphene (on top of monolayer graphene) considering the ~0.3

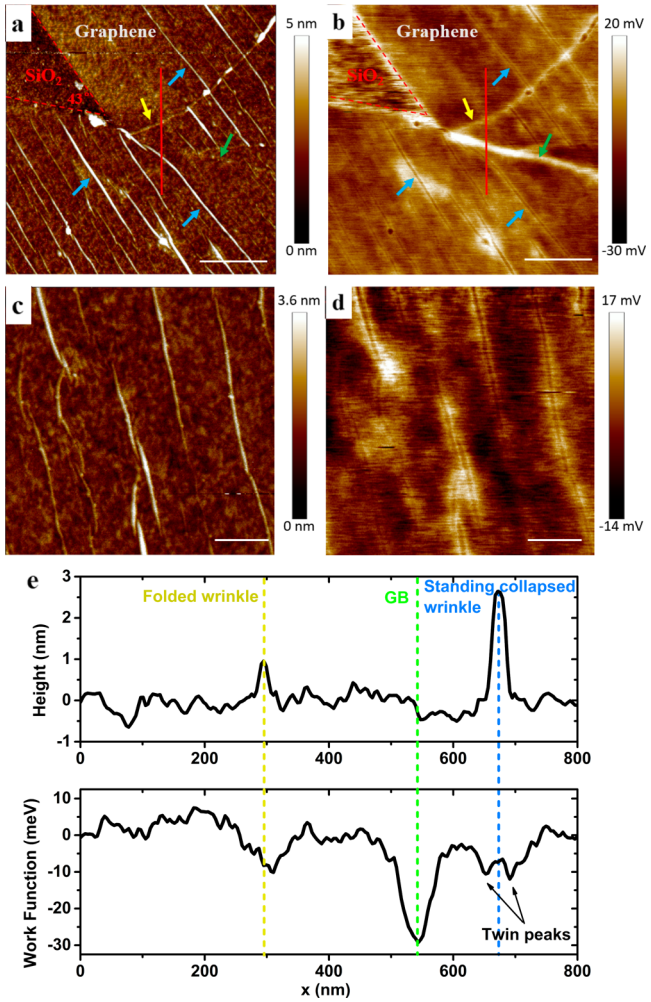

Figure 3. (a) AFM topography and (b) KPFM mapping of monolayer graphene on Si/SiO_2 substrate. The tilt angle between the edges of the two grains is 43°. Standing collapsed wrinkles, folded wrinkles, and GBs are indicated by blue, yellow, and green arrows, respectively. (c) AFM topography and (d) KPFM mapping of standing collapsed wrinkles with various sizes. (e) The cross section line profiles indicated by the red line in (a) and (b). The dashed lines indicate the locations of folded wrinkle, GB, and standing collapsed wrinkle, respectively, with color coding corresponding to that in (a) and (b). Scale bars in (a) and (b) are 500 nm, and in (c) and (d) are 200 nm.

DOI: 10.1021/acsami.6b04853
ACS Appl. Mater. Interfaces 2016, 8, 18360−18366

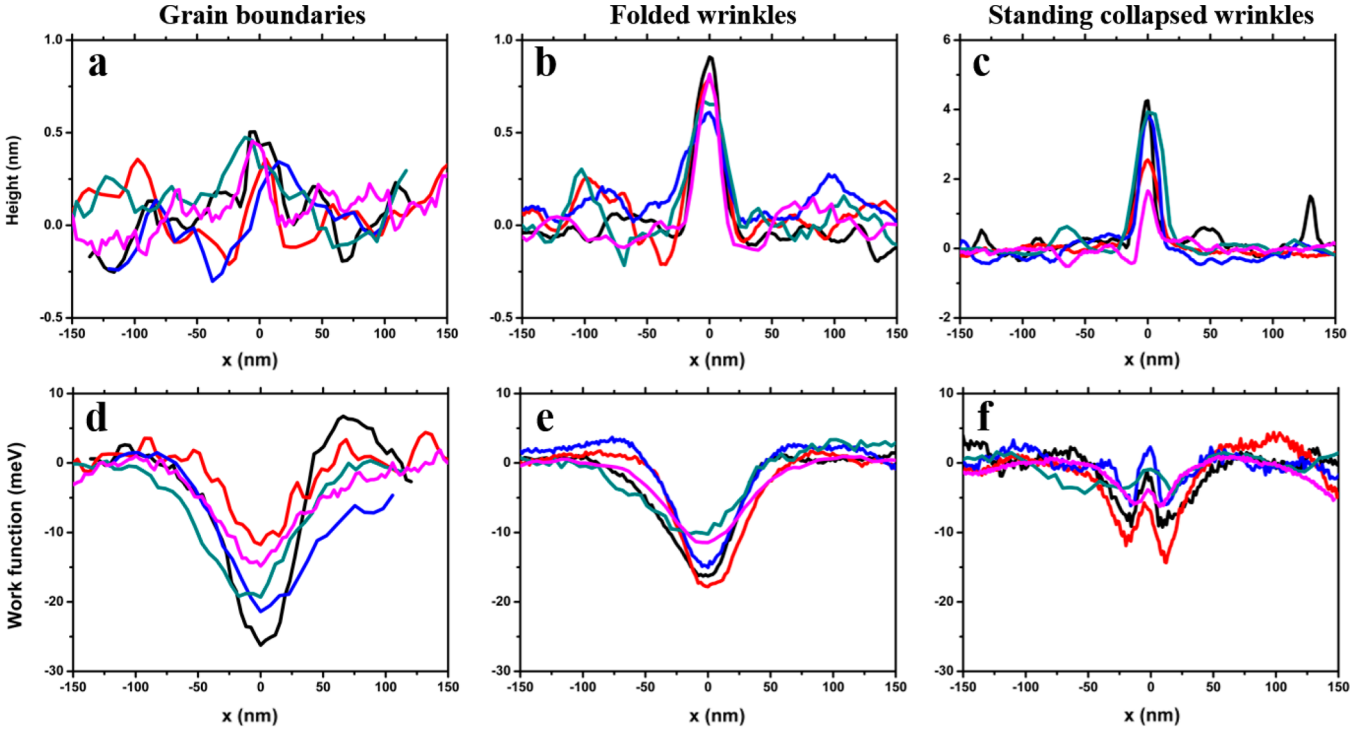

Figure 4. (a–c) Height profiles of GBs, folded wrinkles, and standing collapsed wrinkles, respectively. Four profiles for each type of defects are displayed and coded with color. (d–f) The corresponding work function profiles are displayed. The vertical coordinates of work function profiles are set to the same value in order to emphasize the characteristic patterns. Each profile is averaged along the length of the defect to reduce noise.

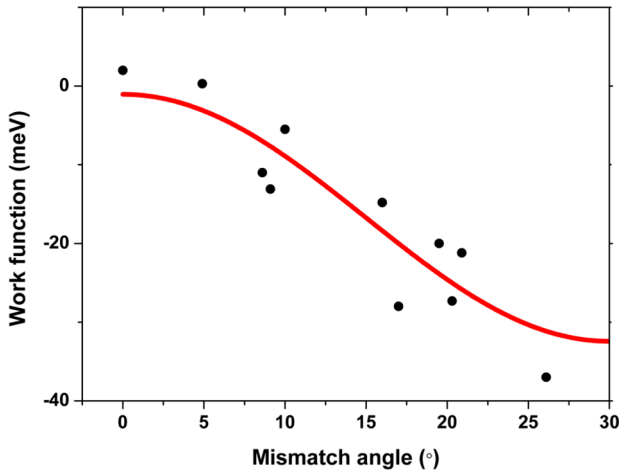

Figure 5. Work function change at GBs with various stitching angles. Considering the 6-fold symmetry of graphene sheets with honeycomb bonding structure, the stitching angle is measured from 0° to 30°, where 30° corresponds to the largest stitching angle.[24] Accordingly, the data are fitted with a sinusoidal curve with $\pi/3$ period (red solid line).

nm roughness of our sample. Therefore, it is reasonable to assume that this defect has the "folded wrinkle" structure. In addition to wrinkles, GBs are also expected to form at the boundary between the two grains. It has been reported by STM experiment that the average height of GBs is around 0.19 nm.[11] This is within the surface roughness of our sample, making the GBs difficult to be resolved in AFM topography as indicated by the green arrow. As one can see, the topography of these defects is very similar, especially for the folded wrinkles and GBs with only subnanometer variation in height. This morphological similarity may lead to inaccurate identifications of line defects.

On the other hand, the KPFM image in Figure 3b shows characteristic patterns of standing collapsed wrinkles, folded wrinkles, and GBs, respectively, with corresponding colored arrows pointing to the same featured positions. The standing collapsed wrinkles are displayed as bright lines at both of their edges and darker contrast in the center part along the axial direction. Note that in our experiment, brighter contrast represents lower work function. This suggests that the work function values have been increased at the center of wrinkle while decreased at both edges. This "twin peaks" effect is more obvious for taller wrinkles than shorter ones, as illustrated in Figure 3c and d. For the folded wrinkles, it is not convincing to identify their types only from topography data. Interestingly, their work functions are lower than the defect free graphene (brighter contrast in KPFM mapping) which can be attributed to the multilayer nature of their atomic structures as will be discussed later. Moreover, folded wrinkles are usually longer than the standing collapsed wrinkles, even spanning across the whole single grain with tens of microns in length (see Supporting Information Figure S1). For GBs, although not obviously resolved in topography, they demonstrate sharp contrast in the KPFM mapping with decreased work function than the defect free area of graphene. In summary, each type of line defects exhibit characteristic work function variations. On the basis of this observation, we propose a combination of topography and KPFM data as an easy-to-use and non-destructive method for confident identification of graphene line defects (see Figure S2).

Figure 3e demonstrates the line profiles across all three types of defects. From the topography profile, the standing collapsed wrinkle is 2.61 nm high, and the folded wrinkle is 0.95 nm. But it is difficult to resolve the grain boundary. On the other hand,

DOI: 10.1021/acsami.6b04853
ACS Appl. Mater. Interfaces 2016, 8, 18360–18366

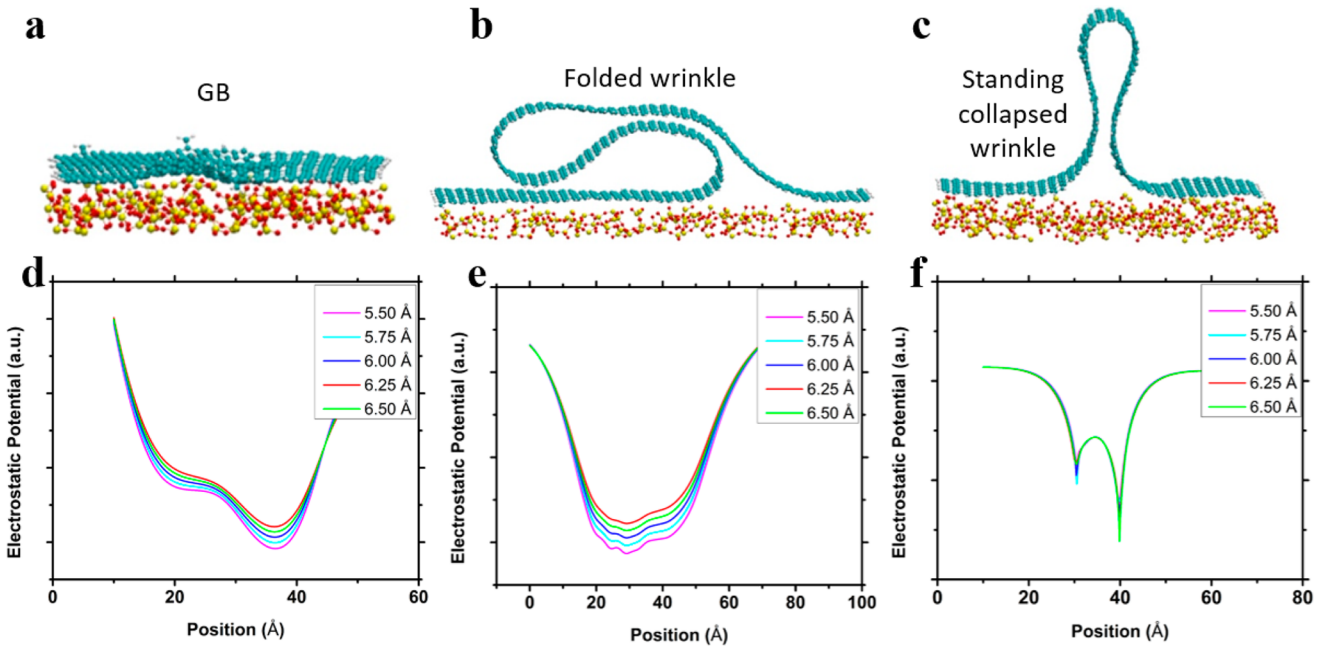

Figure 6. (a–c) Molecular dynamics simulation system for GB, folded wrinkle, and standing collapsed wrinkle, respectively. The carbon, silicon, and oxygen atoms are represented in cyan, yellow, and red, respectively. (d–f) The corresponding calculated electrostatic potentials at various separations above the sample surface. The simulation results are very similar to the characteristic work function variation observed with KPFM in Figure 4.

there is a pronounced peak of −27.2 meV corresponding to grain boundary, and a lower peak of −12.4 meV corresponding to the folded wrinkle. Meanwhile, the "twin peaks" of −10.4 and −8.8 meV at the edges of the standing collapsed wrinkle resulted from the work function decrease at both edges and increase at the center of the wrinkle as discussed previously.

To better illustrate the characteristic work function variations of the line defects, we measured the topography and KPFM profiles of line defects from various samples. Figure 4a–c show the height profiles of GBs, folded wrinkles, and standing collapsed wrinkles, respectively. Each figure contains four data sets selected from different samples and coded with color. Figure 4d–f depict the corresponding work function profiles. Each profile curve is averaged along the axial direction of the defect to reduce background noise. In Figure 4a, the height profiles of the GBs are almost buried in the surface roughness and the average height is within 0.5 nm; meanwhile the work function shows obvious decrease from −13.1 to −27.3 meV compared to the defect free graphene as shown in Figure 4d. The height of folded wrinkles shows less variation, and the average is 0.84 nm as shown in Figure 4b. This height value is close to the theoretical value of double-layer graphene (on top of monolayer graphene) considering the 0.3 nm surface roughness. In Figure 4e, the work function decrease of the folded wrinkles is 9.0–16.1 meV. The standing collapsed wrinkles are much taller with height 1.6–4.6 nm in Figure 4c, while the work function profiles show very characteristic "twin peaks" patterns, in which the work function decreases at the wrinkle edges and increases along the axial center, as illustrated in Figure 4f. From Figure 4, we can see that with the combination of topography and KPFM mapping, GBs, standing collapsed wrinkles, and folded wrinkles can be identified by their characteristic patterns.

We also noticed that the work function variation of both types of wrinkles is relatively consistent, while that of GBs varies from sample to sample. We believe this variation in GBs is due to the different stitching angle between adjacent grains. To test this hypothesis, we synthesized GBs with different stitching angles and measured the corresponding work functions, as shown in Figure 5. For small stitching angles ($\theta \rightarrow 0°$), the work function is close to that of defect free graphene. Meanwhile, for large stitching angles ($\theta \rightarrow 30°$), the work function decreases dramatically to −37 meV. This clear trend of work function variation agrees well with the increasing density of defects at GBs with large stitching angles.[32] The data can also be well fitted with a sinusoidal curve with a $\pi/3$ period, as one would physically expect from a 6-fold graphene symmetry.

To gain insight into the origin of the characteristic work function variations of graphene line defects, classical and quantum molecular dynamics simulations are performed on graphene with a GB, folded wrinkle, and standing collapsed wrinkle, respectively. The modeling systems are shown in Figure 6a–c, where the edges are passivated by hydrogen atoms. All the line defects are deposited on amorphous SiO_2. The GB has mismatch angle of 18°, the folded wrinkle has height of 18 Å and that of the standing collapsed wrinkle is 32 Å. The corresponding calculated electrostatic potentials are shown in Figure 6d–f. The curves at various separation above the defects from 5.5–6.5 Å are prestented. The simulation curves for each type of line defects in Figure 6d–f show very similar characteristic variations with those observed by KPFM as shown in Figure 4d–f. This confirms that the work function variations observed by KPFM are originated from the intrinsic electrical properties of line defects, instead of imaging artifacts induced by morphology.

From the simulation results, we conclude that the characteristic work function variations can be attributed to the electrical interaction between graphene and SiO_2 substrate.[21,33] For GB shown in Figure 6a and d, the presence of nonhexagonal defects

DOI: 10.1021/acsami.6b04853
ACS Appl. Mater. Interfaces 2016, 8, 18360–18366

introduces localized states, which decreases GB work function, leading to $p-p'-p$ ($p' < p$) potential barriers.[5] This is in good agreement with atomic-resolution STM observations.[11] For folded wrinkle shown in Figure 6b and e, due to the multilayer atomic structure, the Fermi level shift is lower than the monolayer graphene,[21] which introduces the lower work function. For standing collapsed wrinkles, the characteristic "twin peaks" work function variation is a result of both doping and morphology. First, single layer graphene is *p*-doped on SiO_2 substrate in ambient air. With increasing gap between graphene and substrate, the doping effect is prohibited.[18] Therefore, at the edges of the standing collapsed wrinkle, the work functions are lower than the wrinkle free graphene. Along the axial center of wrinkles where the gap between graphene and substrate is at maximum, the work function is expected to be minimum according to the doping theory. However, when probing the electrostatic potential from above the sample, the measured values are the sum of all the potential of the carbon atoms underneath. Given the morphology of standing collapsed wrinkle, there are fewer carbon atoms at the top than at the edges. This in effect leads to the lower potential at both edges, and also the local maxima at the top of the wrinkle. All the simulation results are in good agreement with KPFM observations.

4. CONCLUSIONS

In summary, line defects are currently inevitable in graphene grown by CVD method and are believed to affect electrical and mechanical properties of polycrystalline graphene. Such defects include wrinkles and GBs. Wrinkles can be further categorized into standing collapsed wrinkles and folded wrinkles. We successfully resolved each of these line defects using KPFM. The characteristic work function variation of each line defect was investigated and the results are in good agreement with both theoretical calculations and experimental results obtained by other microscopic techniques. Our results not only provide an easy-to-use and accurate method for graphene line defects detection, but also show the potential to tune the graphene work function by defects engineering.

■ ASSOCIATED CONTENT

Supporting Information

The Supporting Information is available free of charge on the ACS Publications website at DOI: 10.1021/acsami.6b04853.

Additional experimental data and analysis graphs (PDF)

■ AUTHOR INFORMATION

Corresponding Authors

*E-mail: Salehikh@uic.edu.
*E-mail: rsyassar@uic.edu.

Author Contributions

Authors F.L. and R.S.Y. conceived the idea. F.L. and W.T.Y. performed KPFM measurements and R.S.Y supervised them. P.Y. synthesized graphene samples, performed SEM and Raman characterizations, and A.S.K supervised him. R.S. performed the MD simulations and P.K. supervised him. All authors have given approval to the final version of the manuscript.

Notes

The authors declare no competing financial interest.

■ ACKNOWLEDGMENTS

R.S.Y., F.L., and W.T.Y. acknowledge financial support from the National Science Foundation (Award DMR-1410560). A.S.K. and P.Y. acknowledge the financial support from the National Science Foundation (EFMA-1542864). P.K. and R.S. acknowledge the financial support from the National Science Foundation Division of Materials Research grant 1309765.

■ REFERENCES

(1) Yazyev, O. V.; Chen, Y. P. Polycrystalline Graphene and Other Two-Dimensional Materials. *Nat. Nanotechnol.* **2014**, *9*, 755−767.
(2) Lahiri, J.; Lin, Y.; Bozkurt, P.; Oleynik, I. I.; Batzill, M. An Extended Defect in Graphene as a Metallic Wire. *Nat. Nanotechnol.* **2010**, *5*, 326−329.
(3) Yazyev, O. V.; Louie, S. G. Electronic Transport in Polycrystalline Graphene. *Nat. Mater.* **2010**, *9*, 806−809.
(4) Yu, Q.; Jauregui, L. A.; Wu, W.; Colby, R.; Tian, J.; Su, Z.; Cao, H.; Liu, Z.; Pandey, D.; Wei, D.; Chung, T. F.; Peng, P.; Guisinger, N. P.; Stach, E. A.; Bao, J.; Pei, S.-S.; Chen, Y. P. Control and Characterization of Individual Grains and Grain Boundaries in Graphene Grown by Chemical Vapour Deposition. *Nat. Mater.* **2011**, *10*, 443−449.
(5) Yasaei, P.; Kumar, B.; Hantehzadeh, R.; Kayyalha, M.; Baskin, A.; Repnin, N.; Wang, C.; Klie, R. F.; Chen, Y. P.; Král, P.; Salehi-Khojin, A. Chemical Sensing with Switchable Transport Channels in Graphene Grain Boundaries. *Nat. Commun.* **2014**, *5*, 4911.
(6) Liu, Y.; Yakobson, B. I. Cones, Pringles, and Grain Boundary Landscapes in Graphene Topology. *Nano Lett.* **2010**, *10*, 2178−2183.
(7) Hattab, H.; N'Diaye, A. T.; Wall, D.; Klein, C.; Jnawali, G.; Coraux, J.; Busse, C.; van Gastel, R.; Poelsema, B.; Michely, T.; Meyer zu Heringdorf, F.-J.; Horn-von Hoegen, M. Interplay of Wrinkles, Strain, and Lattice Parameter in Graphene on Iridium. *Nano Lett.* **2012**, *12*, 678−682.
(8) Paronyan, T. M.; Pigos, E. M.; Chen, G.; Harutyunyan, A. R. Formation of Ripples in Graphene as a Result of Interfacial Instabilities. *ACS Nano* **2011**, *5*, 9619−9627.
(9) Zhang, Y.; Gao, T.; Gao, Y.; Xie, S.; Ji, Q.; Yan, K.; Peng, H.; Liu, Z. Defect-Like Structures of Graphene on Copper Foils for Strain Relief Investigated by High-Resolution Scanning Tunneling Microscopy. *ACS Nano* **2011**, *5*, 4014−4022.
(10) Zhu, W.; Low, T.; Perebeinos, V.; Bol, A. A.; Zhu, Y.; Yan, H.; Tersoff, J.; Avouris, P. Structure and Electronic Transport in Graphene Wrinkles. *Nano Lett.* **2012**, *12*, 3431−3436.
(11) Koepke, J. C.; Wood, J. D.; Estrada, D.; Ong, Z.-Y.; He, K. T.; Pop, E.; Lyding, J. W. Atomic-Scale Evidence for Potential Barriers and Strong Carrier Scattering at Graphene Grain Boundaries: A Scanning Tunneling Microscopy Study. *ACS Nano* **2013**, *7*, 75−86.
(12) Huang, P. Y.; Ruiz-Vargas, C. S.; van der Zande, A. M.; Whitney, W. S.; Levendorf, M. P.; Kevek, J. W.; Garg, S.; Alden, J. S.; Hustedt, C. J.; Zhu, Y.; Park, J.; McEuen, P. L.; Muller, D. A. Grains and Grain Boundaries in Single-Layer Graphene Atomic Patchwork Quilts. *Nature* **2011**, *469*, 389−392.
(13) Kim, K.; Lee, Z.; Regan, W.; Kisielowski, C.; Crommie, M. F.; Zettl, A. Grain Boundary Mapping in Polycrystalline Graphene. *ACS Nano* **2011**, *5*, 2142−2146.
(14) Kim, D. W.; Kim, Y. H.; Jeong, H. S.; Jung, H.-T. Direct Visualization of Large-Area Graphene Domains and Boundaries by Optical Birefringency. *Nat. Nanotechnol.* **2011**, *7*, 29−34.
(15) Duong, D. L.; Han, G. H.; Lee, S. M.; Gunes, F.; Kim, E. S.; Kim, S. T.; Kim, H.; Ta, Q. H.; So, K. P.; Yoon, S. J.; Chae, S. J.; Jo, Y. W.; Park, M. H.; Chae, S. H.; Lim, S. C.; Choi, J. Y.; Lee, Y. H. Probing Graphene Grain Boundaries with Optical Microscopy. *Nature* **2012**, *490*, 235−239.
(16) Yu, S. U.; Park, B.; Cho, Y.; Hyun, S.; Kim, J. K.; Kim, K. S. Simultaneous Visualization of Graphene Grain Boundaries and Wrinkles with Structural Information by Gold Deposition. *ACS Nano* **2014**, *8*, 8662−8668.

DOI: 10.1021/acsami.6b04853
ACS Appl. Mater. Interfaces 2016, 8, 18360−18366

(17) Nonnenmacher, M.; O'Boyle, M. P.; Wickramasinghe, H. K. Kelvin Probe Force Microscopy. *Appl. Phys. Lett.* **1991**, *58*, 2921−2923.
(18) Kazakova, O.; Panchal, V.; Burnett, T. Epitaxial Graphene and Graphene−Based Devices Studied by Electrical Scanning Probe Microscopy. *Crystals* **2013**, *3*, 191.
(19) Datta, S. S.; Strachan, D. R.; Mele, E. J.; Johnson, A. T. C. Surface Potentials and Layer Charge Distributions in Few-Layer Graphene Films. *Nano Lett.* **2009**, *9*, 7−11.
(20) Yu, Y.-J.; Zhao, Y.; Ryu, S.; Brus, L. E.; Kim, K. S.; Kim, P. Tuning the Graphene Work Function by Electric Field Effect. *Nano Lett.* **2009**, *9*, 3430−3434.
(21) Ziegler, D.; Gava, P.; Güttinger, J.; Molitor, F.; Wirtz, L.; Lazzeri, M.; Saitta, A. M.; Stemmer, A.; Mauri, F.; Stampfer, C. Variations in the Work Function of Doped Single- and Few-Layer Graphene Assessed by Kelvin Probe Force Microscopy and Density Functional Theory. *Phys. Rev. B: Condens. Matter Mater. Phys.* **2011**, *83*, No. 235434.
(22) Colchero, J.; Gil, A.; Baró, A. M. Resolution Enhancement and Improved Data Interpretation in Electrostatic Force Microscopy. *Phys. Rev. B: Condens. Matter Mater. Phys.* **2001**, *64*, No. 245403.
(23) Vlassiouk, I.; Regmi, M.; Fulvio, P.; Dai, S.; Datskos, P.; Eres, G.; Smirnov, S. Role of Hydrogen in Chemical Vapor Deposition Growth of Large Single-Crystal Graphene. *ACS Nano* **2011**, *5*, 6069−6076.
(24) Yasaei, P.; Fathizadeh, A.; Hantehzadeh, R.; Majee, A. K.; El-Ghandour, A.; Estrada, D.; Foster, C.; Aksamija, Z.; Khalili-Araghi, F.; Salehi-Khojin, A. Bimodal Phonon Scattering in Graphene Grain Boundaries. *Nano Lett.* **2015**, *15*, 4532−4540.
(25) Phillips, J. C.; Braun, R.; Wang, W.; Gumbart, J.; Tajkhorshid, E.; Villa, E.; Chipot, C.; Skeel, R. D.; Kalé, L.; Schulten, K. Scalable Molecular Dynamics with Namd. *J. Comput. Chem.* **2005**, *26*, 1781−1802.
(26) Humphrey, W.; Dalke, A.; Schulten, K. Vmd: Visual Molecular Dynamics. *J. Mol. Graphics* **1996**, *14*, 33−38.
(27) MacKerell, A. D.; Bashford, D.; Bellott, M.; Dunbrack, R. L.; Evanseck, J. D.; Field, M. J.; Fischer, S.; Gao, J.; Guo, H.; Ha, S.; Joseph-McCarthy, D.; Kuchnir, L.; Kuczera, K.; Lau, F. T. K.; Mattos, C.; Michnick, S.; Ngo, T.; Nguyen, D. T.; Prodhom, B.; Reiher, W. E.; Roux, B.; Schlenkrich, M.; Smith, J. C.; Stote, R.; Straub, J.; Watanabe, M.; Wiórkiewicz-Kuczera, J.; Yin, D.; Karplus, M. All-Atom Empirical Potential for Molecular Modeling and Dynamics Studies of Proteins. *J. Phys. Chem. B* **1998**, *102*, 3586−3616.
(28) Darden, T.; York, D.; Pedersen, L. Particle Mesh Ewald: An N·Log(N) Method for Ewald Sums in Large Systems. *J. Chem. Phys.* **1993**, *98*, 10089−10092.
(29) Kästner, J.; Carr, J. M.; Keal, T. W.; Thiel, W.; Wander, A.; Sherwood, P. Dl-Find: An Open-Source Geometry Optimizer for Atomistic Simulations. *J. Phys. Chem. A* **2009**, *113*, 11856−11865.
(30) Ufimtsev, I. S.; Martinez, T. J. Quantum Chemistry on Graphical Processing Units. 3. Analytical Energy Gradients, Geometry Optimization, and First Principles Molecular Dynamics. *J. Chem. Theory Comput.* **2009**, *5*, 2619−2628.
(31) Grimme, S.; Antony, J.; Ehrlich, S.; Krieg, H. A Consistent and Accurate Ab Initio Parametrization of Density Functional Dispersion Correction (Dft-D) for the 94 Elements H-Pu. *J. Chem. Phys.* **2010**, *132*, 154104.
(32) Grantab, R.; Shenoy, V. B.; Ruoff, R. S. Anomalous Strength Characteristics of Tilt Grain Boundaries in Graphene. *Science* **2010**, *330*, 946−948.
(33) Filleter, T.; Emtsev, K. V.; Seyller, T.; Bennewitz, R. Local Work Function Measurements of Epitaxial Graphene. *Appl. Phys. Lett.* **2008**, *93*, 133117.

DOI: 10.1021/acsami.6b04853
ACS Appl. Mater. Interfaces 2016, 8, 18360−18366